

G64.5+0.9, a new shell supernova remnant with unusual central emission^{*}

AMI CONSORTIUM: Natasha Hurley-Walker[†], Matthew L. Davies,
 Thomas M. O. Franzen, Keith Grainge, D. A. Green, Michael P. Hobson,
 Anthony Lasenby, Guy Pooley, Carmen Rodríguez-Gonzálvez,
 Richard D. E. Saunders, A. M. M. Scaife, Paul F. Scott, Timothy Shimwell,
 David Titterton, Elizabeth Waldram and Jonathan T. L. Zwart
Astrophysics Group, Cavendish Laboratory, 19 J. J. Thomson Avenue, Cambridge CB3 0HE

Accepted —; received —; in original form 17 November 2018

ABSTRACT

We present observations between 1.4 and 18 GHz confirming that G64.5+0.9 is new Galactic shell supernova remnant, using the Very Large Array and the Arcminute Microkelvin Imager. The remnant is a shell $\simeq 8'$ in diameter with a spectral index of $\alpha = 0.47 \pm 0.03$ (with α defined such that flux density S varies with frequency ν as $S \propto \nu^{-\alpha}$). There is also emission near the centre of the shell, $\simeq 1'$ in extent, with a spectral index of $\alpha = 0.81 \pm 0.02$. We do not find any evidence for spectral breaks for either source within our frequency range. The nature of the central object is unclear and requires further investigation, but we argue that is most unlikely to be extragalactic. It is difficult to avoid the conclusion that it is associated with the shell, although its spectrum is very unlike that of known pulsar wind nebulae.

Key words: supernova remnants – radio continuum: ISM – radiation mechanisms: non-thermal

1 INTRODUCTION

While examining an NRAO VLA Sky Survey (NVSS) image (Condon et al. 1998) of the region surrounding the Galactic supernova remnant G63.7+1.1, an arc of extended emission was noticed near RA= $19^{\text{h}}50^{\text{m}}24^{\text{s}}$, Dec= $28^{\circ}16'25''$ (see Fig. 1). As it resembles part of a ring and lies in the Galactic plane, it was identified as a possible supernova remnant (SNR). Tian and Leahy 2006 also noticed this structure in Canadian Galactic Plane Survey (CGPS; Taylor et al. 2003) data with similar sensitivity to but poorer resolution than the NVSS data, and proposed it as a possible SNR. It has now been observed with the VLA and the newly commissioned Arcminute Microkelvin Imager (AMI; see AMI Consortium: Zwart et al. 2008). These observations are described in Section 2, and calibration and data reduction in Section 3. Results are presented in Section 4, and we analyse and discuss all available data in Section 5, confirming G64.5+0.9 as a new Galactic SNR.

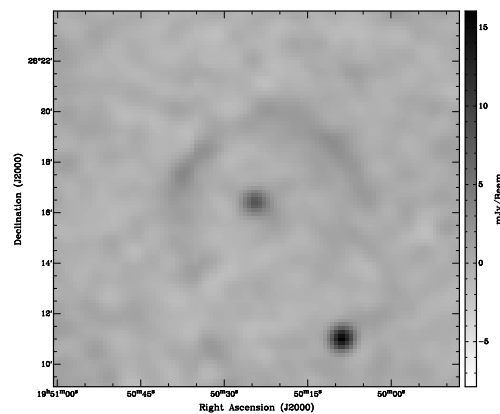


Figure 1. NVSS image of G64.5+0.9; the resolution is 45 arcseconds and the map noise is 3 mJy beam^{-1} .

2 OBSERVATIONS

The position of the source close on the sky to the ring centre was chosen as the pointing centre for observations with the VLA and AMI. AMI is a dual set of interferometric arrays located at the Mullard Radio Astronomy Observatory, Lord’s Bridge, Cambridge, UK. The AMI Small Array (SA) consists of ten 3.7-m diameter

^{*} We request that any reference to this paper cites “AMI Consortium: Hurley-Walker et al. 2009”

[†] Issuing author; E-mail: nh313@mrao.cam.ac.uk

Table 1. Observations of G64-5+0-9.

Telescope	AMI SA	AMI LA	VLA		
Date	2007 October	2008 October	2008 July		
Flux Calibrator	3C286	3C48	3C48		
Phase Calibrator	J2023+3153	J2023+3153	J1925+211		
Frequency/ GHz	14–18	14–18	1.43	4.86	8.46
Observation(s) Length	16 hours	10 hours	40 minutes	40 minutes	20 minutes
Synthesised beam FWHM	3–2′	1–0.3′	0.75′	0.22′	0.12′
Primary beam FWHM	22–16′	5.6–5.0′	32′	9.3′	5.3′

equatorially-mounted dishes with a baseline range of $\simeq 5 - 20$ m, while the AMI Large Array (LA) has eight 12.8-m-diameter dishes with a baseline range of $\simeq 20 - 100$ m. Both arrays observe I+Q in the band 12–18 GHz, each with system temperatures of about 25 K.

The backends are analogue Fourier transform spectrometers, from which the complex signals in each of eight channels of 750-MHz bandwidth are synthesised, and the signals in the synthesised channels are correlated at the $\simeq 10$ per cent level. In practice, the lowest two frequency channels are generally not used due to a poor correlator response in this frequency range and, currently, interference.

Frequencies, resolutions, dates, calibrators and observing times for each observation are shown in Table 1. The AMI SA observed a single pointing while the AMI LA used a seven-point raster mode with 4′ spacing. J2023+3153 (RA= $20^h23^m19^s.0$, Dec= $31^\circ53′02″.3$) was chosen as a phase calibrator from the Jodrell Bank VLA Survey (JVAS; Patnaik et al. 1992; Browne et al. 1998; Wilkinson et al. 1998) on the basis of its proximity and flux density (1.1 Jy at 15 GHz).

During the time of our VLA observations, about half of the antennas of the VLA were upgraded Extended VLA (EVLA) antennas. This necessitated an extra step of calibration on VLA–EVLA baselines. The telescope was in D-array, and we used the L, C and X band receivers at centre frequencies of 1.43, 4.86 and 8.46 GHz respectively. J1925+211 (RA= $19^h25^m59^s.6$, Dec= $21^\circ06′26″.2$) was selected from the VLA Calibrator Manual¹ as the phase calibrator at 1.43, 4.86 and 8.46 GHz in D-array; it has an assumed flux density of 1.3, 1.5 and 1.0 Jy in each of these bands, respectively.

3 CALIBRATION AND DATA REDUCTION

The AMI data reduction was performed using our software tool REDUCE. This is used to apply path-compensator and path-delay corrections, to flag interference, shadowing and hardware errors, to apply phase and amplitude calibrations and to Fourier transform the correlator data readout to synthesise the frequency channels, before outputting to disk in *uv*-FITS format suitable for imaging in AIPS.

Flux calibration was performed using short observations of 3C48 and 3C286 near the beginning and end of each run, with assumed I + Q flux densities for these sources in the AMI channels consistent with Baars et al. (1977) (see Table 2). As Baars et al. measure I and AMI measures I + Q, these flux densities include corrections for the polarization of the sources derived by interpolating from VLA 5-, 8- and 22-GHz observations. After phase calibration, the phase of AMI over one hour is generally stable to 5° for channels 4–7, and to 10° for channels 3 and 8.

The system temperatures of each AMI antenna are continuously

Table 2. Assumed I + Q flux densities of 3C286 and 3C48 over the commonly-used AMI band.

Channel	ν /GHz	S^{3C286} /Jy	S^{3C48} /Jy
3	14.2	3.61	1.73
4	15.0	3.49	1.65
5	15.7	3.37	1.57
6	16.4	3.26	1.49
7	17.1	3.16	1.43
8	17.9	3.06	1.37

monitored using a modulated noise signal injected at each antenna; this is used to continuously correct the amplitude scale in a frequency-independent way. The overall consistency of the flux-density scale is estimated to be better than 5 per cent.

Since the AMI antennas are sensitive to I+Q and are equatorially mounted, this polarization is fixed on the sky during the observation. Q may be positive or negative, but is expected to be small when integrated over the whole source.

VLA data reduction was performed entirely within AIPS. The VLA–EVLA baselines were also calibrated using BLCAL as described in the guidelines for post-processing EVLA data in AIPS². This corrects for closure errors on these baselines caused by non-matched EVLA and VLA bandpass shapes.

Maps were made using IMAGR in AIPS from each channel of the AMI SA, AMI LA and the VLA (Fig. 2). Combined-channel maps of the AMI SA and AMI LA observations are shown in Fig. 3 and Fig. 4, respectively. The VLA and AMI SA images shown are not corrected for the primary beams of the telescopes, but when measuring flux densities this correction is made. In order to produce a raster map, the AMI LA images are of course primary-beam corrected. The signal-to-noise of the 1.43-GHz image was large enough that self-calibration from the first non-negative CLEAN components was used to enhance the image.

4 RESULTS

We note that the maps show two sources of emission: a ring-like structure surrounding a slightly extended, apparently central object. In those maps that do not resolve the ring completely, the emission from these two sources may be confused.

As we are using interferometers sensitive to a limited range of angular scales, it is not possible to obtain accurate flux densities for structures on all scales from all of the observations. Only the VLA 1.43-GHz and AMI SA observations have the required short baselines to provide sensitivity to the extended ring emission. The AMI SA does not have the required resolution to measure the flux density of the central emission without confusion with the ring.

To measure flux density, we adopt the fitting method of Green

¹ <http://www.aoc.nrao.edu/~gtaylor/csource.html>

² <http://www.vla.nrao.edu/astro/guides/evlareturn/postproc.shtml>

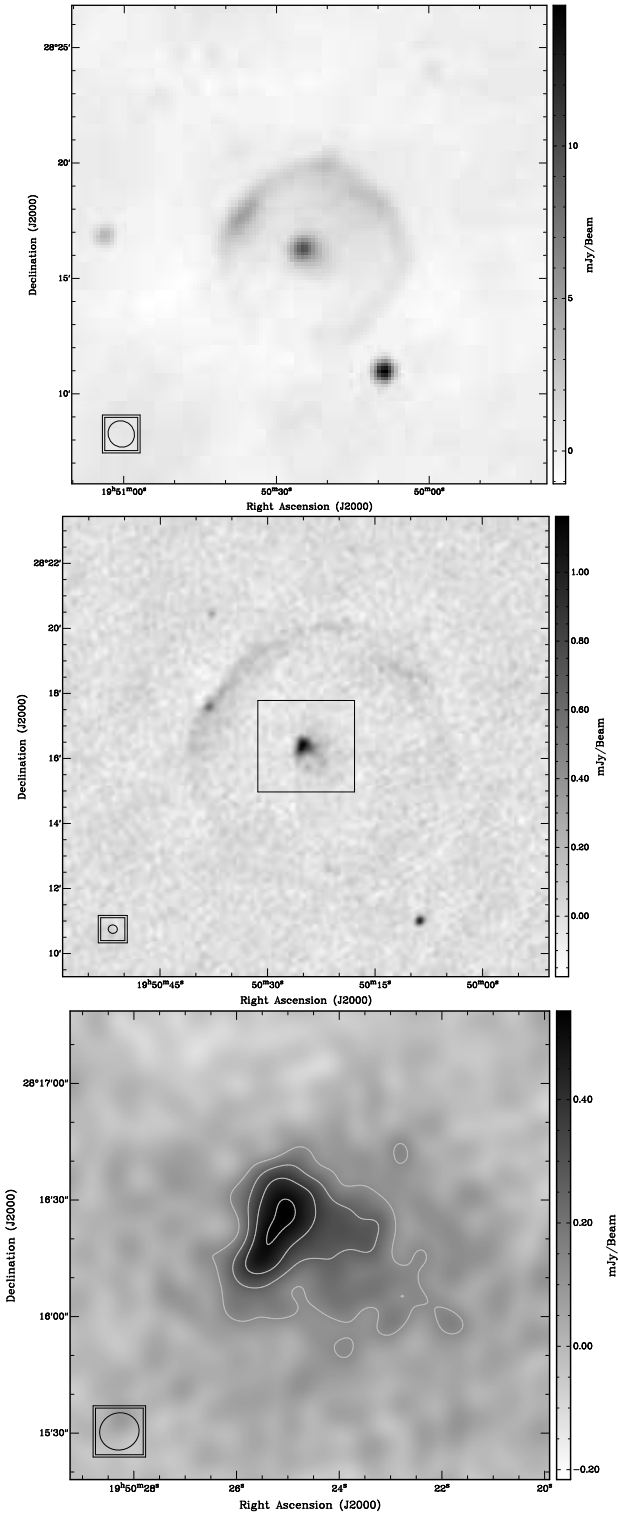


Figure 2. VLA images of G64.5+0.9. Top: 1.43 GHz, $\sigma_{rms} = 110 \mu\text{Jy beam}^{-1}$, uniform weighting; middle: 4.86 GHz, $\sigma_{rms} = 38.5 \mu\text{Jy beam}^{-1}$, uniform weighting; bottom: 8.46 GHz, $\sigma_{rms} = 43.5 \mu\text{Jy beam}^{-1}$, natural weighting with three-sigma contours. The box in the middle panel indicates the area that is shown in the lower panel. In this and subsequent images, the FWHM of the CLEAN restoring beam of the observation is shown as an ellipse inside a box on the lower left.

(2007), using the program FITFLUX. In this method, a flux density is fitted by drawing a polygon around the object and fitting a tilted plane to the pixels around the edges of the polygon. The tilted plane is then removed from the image before integrating the emission within the polygon. This method is sensitive to the fitting area selected but only at the one per cent level, which is included in the estimate of the error. This method allows us to remove contribution from the background, especially the contribution from the ring in the case of measuring the flux density of the central emission.

The main sources of error on the flux density measurements are the thermal noise σ_{rms} and the error on the flux calibration σ_S . Long-term measurements of the AMI flux calibration show it to have an r.m.s. error of three per cent. The VLA flux calibration is performed using GETJY which scales the fluxes of the field and phase calibrator using the flux density of 3C48 consistent with Baars et al.. This process has an error of less than one per cent for each of the frequency channels. Therefore to obtain the error on a flux density measurement, the thermal noise of each map is added in quadrature with the flux calibration error of the telescope used, and a one per cent error when FITFLUX is used.

We now discuss the results from each observation in turn.

4.1 VLA 1.43 GHz

Fig. 2 shows that this object is clearly a shell SNR, brighter in the north-east. Interestingly, the central emission is also brightest in this direction. The full ring structure is clearly discernable in this map, as compared to the partial structure shown in the NVSS map (Fig. 1). This is due to the enhanced uv coverage and lower noise of the longer pointed observation.

FITFLUX was used to obtain the flux density of the central object as $17.1 \pm 0.8 \text{ mJy}$, and the flux density of the entire remnant as $119 \pm 5 \text{ mJy}$. The former was subtracted from the latter to obtain the flux density of the ring as $102 \pm 5 \text{ mJy}$.

4.2 VLA 4.85 GHz

At 4.85 GHz, the ring is resolved out to the extent that it is not possible to extract a reliable estimate of its integrated flux density. However, the structure of the emission close to the ring centre becomes more clear; its integrated flux density is listed in Table 3.

The north-east section of the ring shows possible contamination with a point source. Using the AIPS routine SLICE, a cross-sectional profile across this source, perpendicular to a tangent along the ring at this point, was produced in order to measure the flux levels. The base flux level from the ring is $220 \mu\text{Jy beam}^{-1}$ and the peak point source flux is $620 \mu\text{Jy beam}^{-1}$. The width of the source profile at $420 \mu\text{Jy beam}^{-1}$ is $12''$, which is the resolution of the telescope at this frequency. Therefore the source is unresolved and we postulate it is a background contaminating source. FITFLUX gives a flux density estimate of $0.41 \pm 0.04 \text{ mJy}$ for this source.

4.3 VLA 8.46 GHz

At 8.46 GHz, the ring is almost entirely resolved out. However we obtain good information on the structure of the near-central emission, as shown in the lowest panel of Fig. 2. FITFLUX gives a measurement of the flux density of this source, shown in Table 3.

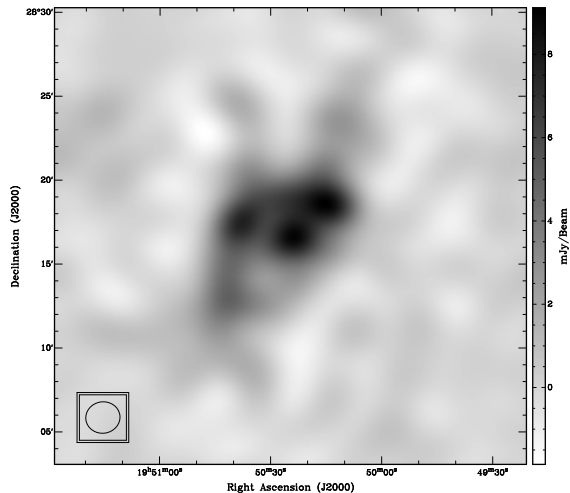


Figure 3. AMI SA combined-channel (14–18 GHz) image of G64.5+0.9; the map noise is $192 \mu\text{Jy beam}^{-1}$.

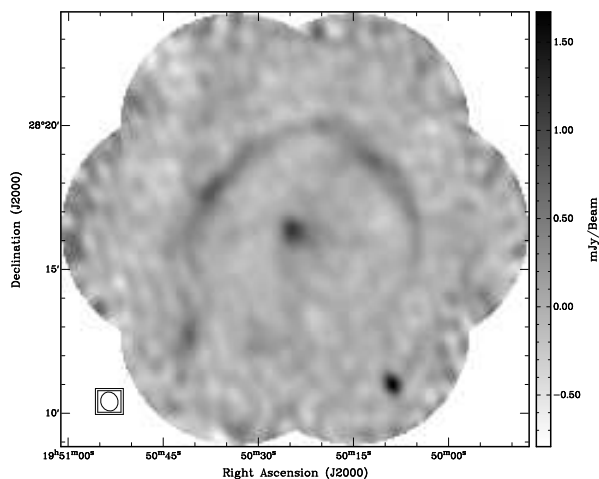


Figure 4. Map of a primary-beam-corrected combined-channel (14–18 GHz) seven-point raster of G64.5+0.9 observed by the AMI LA. The central pointing has a thermal noise of $32 \mu\text{Jy beam}^{-1}$ and the surrounding six pointings have a thermal noise of $58 \mu\text{Jy beam}^{-1}$.

4.4 AMI 14–18 GHz

The AMI SA, due to its sensitivity to larger angular scales, picks up much more large-scale Galactic emission in the region (see Section 4.5 and Fig. 3). The north-east part of the ring structure is clear but is confused with the central source.

The AMI LA combined-channel raster map is shown in Fig. 4. The ring is slightly resolved out by the AMI LA, but the source apparently near the centre shows up clearly and has similar structure to that in the VLA maps at lower frequency. FITFLUX was used to find the flux density of this near-central emission for each channel and these results are listed in Table 3. It is possible that the AMI LA is slightly resolving out this object at the higher end of its frequency coverage. However the slight drop in flux density is within the error bars.

FITFLUX was used to find the flux density of the whole object from the AMI SA combined-channel map, and the flux density of the central source from the AMI LA combined-channel map. These were $35.3 \pm 1.4 \text{ mJy}$ and $2.49 \pm 0.10 \text{ mJy}$, respectively. The latter

Table 3. VLA and AMI LA I+Q flux densities of the emission close to the ring centre.

ν/GHz	S_{ν}/mJy
1.43	17.07 ± 0.36
4.86	7.92 ± 0.16
8.46	4.01 ± 0.08
14.2	2.69 ± 0.17
15.0	2.58 ± 0.12
15.7	2.50 ± 0.13
16.4	2.48 ± 0.12
17.1	2.27 ± 0.12
17.9	2.02 ± 0.11

was subtracted from the former to produce an estimate of the flux density of the ring at 16 GHz of $32.8 \pm 1.4 \text{ mJy}$.

4.5 Data from the literature

Most Galactic radio surveys do not possess the required resolution to resolve G64.5+0.9 well, as it is only $8'$ in diameter. The Effelsberg 2.7-GHz survey data (Reich et al. 1984) show a small knot of emission at the SNR's location, and a large amount of emission on broader angular scales. It was not possible to extract meaningful flux densities for the ring and central source from these data.

This object is also covered by the Westerbork Synthesis Radio Telescope Galactic plane survey³ (see e.g. Taylor et al. 1996) at 327 MHz, which provides low-frequency, large-scale information, at a resolution of $1' \times 2'.11$ at this declination. Unfortunately the residual grating ring of a bright, distant source lies directly over the objects of interest.

Infrared data from the Infrared Astronomical Satellite (IRAS; NASA RP-1190 1987) are too low in resolution to provide any useful information about the region. The Second Digitised Sky Survey (DSS2)⁴ shows only foreground stars in the Galaxy. The ATNF Pulsar Catalogue⁵ (see Manchester 2005) shows no pulsars within one degree of the remnant.

5 DISCUSSION

For both the ring and the near-central emission we fit power-law spectra. We define α such that flux density S varies with frequency ν as $S \propto \nu^{-\alpha}$. Spectra were fitted to these data using a Gaussian likelihood function sampled by a Markov Chain Monte Carlo technique. This method copes with asymmetric errors in $\log S$ across the frequency channels and provides an error estimate on the spectral index directly from the posterior distribution.

Using the VLA 1.43 GHz and AMI measurements of the flux density of the ring, we calculate that it has a spectrum with $\alpha = 0.47 \pm 0.03$. The structure and spectral index identify the shell source G64.5+0.9 as a shell SNR. The surface brightness of the SNR at 1 GHz is $\simeq 3 \times 10^{-22} \text{ W m}^{-2} \text{ Hz}^{-1} \text{ sr}^{-1}$, which is faint for known SNRs (in the faintest 10 per cent of identified SNRs - see e.g. Green 2004). This relatively low surface brightness suggests that the remnant is old, but on the other hand, its highly circular shell suggests it is young. (Tian and Leahy 2006) suggest a possible distance of 11 kpc, based on possibly related HI features, at which

³ http://www.ras.ualgary.ca/wsrt_survey.html

⁴ <http://archive.eso.org/dss/dss>

⁵ <http://www.atnf.csiro.au/research/pulsar/psrcat/>

it would have a diameter of ≈ 26 pc. This is not the first SNR visible in NVSS data which has been overlooked (see e.g. G353.9–2.0 identified by Green 2001).

Fitting a spectrum to the data in Table 3, we find that the central emission has a steep spectrum with $\alpha = 0.81 \pm 0.02$ (Fig. 5). This emission is of interest, because of both its apparent position relative to the ring and its structure. It could be a background, unrelated, extragalactic source, or a Galactic source that may or may not be related to the shell remnant.

First we consider a source at redshift z around 0.1. Then its angular size of around $1'$ implies a physical size D of 100 kpc and its luminosity $P_{1.43}$ is around $3 \times 10^{22} \text{ W Hz}^{-1} \text{ sr}^{-1}$ (taking $H_0 = 72 \text{ km s}^{-1} \text{ Mpc}^{-1}$). These values are typical of FR-I (Fanaroff and Riley 1974) twin-jet or tail radio sources powered by jet-producing machines. However the emission is not reminiscent of known twin-jets or tails – particularly at 8 GHz – and the lack of spectral steepening from 1.43 to 18 GHz also tells against it being this type of radio source. A substantially higher redshift for the emission appears ruled out: its structure is very difficult to reconcile with that of a powerful radio source of whatever physical size or orientation, and the emission shows no sign of the synchrotron or inverse-Compton losses associated with the extended regions of powerful sources.

‘Halo’ emission from certain galaxy clusters might resemble the shape of the near-central emission. However, ‘halo’ emission has an extremely steep radio spectrum (see e.g. Brunetti et al. 2008).

The remaining extragalactic possibility would seem to be synchrotron emission from a nearby system of interacting galaxies. At a redshift $z \approx 0.02$, its angular size of around $1'$ implies a physical size D of 20 kpc and its flux density $S_{1.43 \text{ GHz}}$ of 17.1 mJy implies a luminosity $P_{1.43 \text{ GHz}}$ of $1 \times 10^{21} \text{ W Hz}^{-1} \text{ sr}^{-1}$. Thus, this source’s angular size, flux density and structure are consistent with synchrotron emission from two or three interacting galaxies at z of around 0.01 – 0.05.

However, from NVSS source counts⁶, we estimate at 15 per cent the probability of a source of $S_{1.43} \geq 17$ mJy appearing to lie inside the shell of the SNR purely by chance. Thus the probability of *any* extragalactic radio source of this flux density and of such large angular extent, lying within one arcminute of the centre, is minimal.

Turning to possible Galactic sources of emission for the near-central source, chance association along the line-of-sight with thermal Galactic sources such as HII regions is excluded both by the non-thermal radio spectrum of the central source, and its lack of infra-red emission. The location of the extended emission near the centre of the shell suggests that G64.5+0.9 may be a ‘composite’ SNR, i.e. a shell containing a central pulsar wind nebula (PWN) – for example, see G328.1–1.8 (Dickel et al. 2000). However, the radio spectral index of ≈ 0.8 for the central source is considerably larger than expected, since pulsar wind nebulae usually have relatively flat spectral indices at gigahertz frequencies (e.g. Kothes 2008). If the central source is a pulsar wind nebula associated with G64.5+0.9, then it requires a spectral break at below 1.4 GHz, which would be unusual. A low frequency spectral break, at about 1.3 GHz – three times lower than for any other PWN – has been identified in DA 495 (=G65.7+1.2, Kothes et al.). DA 495 is thought to be rather old ($\sim 20,000$ years), whereas the highly circular nature of the shell of G64.5+0.9 suggests it is relatively young.

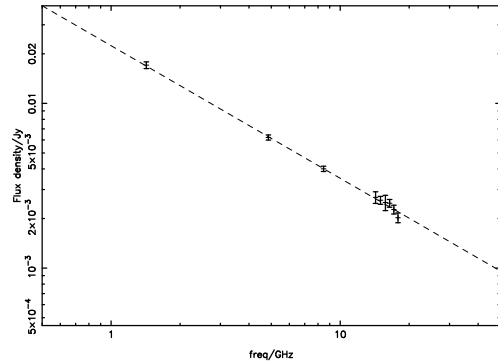


Figure 5. Logarithmic plot of the flux density measurements of the source seen near the centre of G64.5+0.9 in 3. The dashed line indicates a fitted spectrum of $\alpha = 0.81$ using the method described in Section 5.

To identify the nature of this object and fully constrain its association with the remnant, HI absorption-line observations are vital.

6 CONCLUSIONS

Follow-up observations of an arc of emission seen in NVSS and CGPS data have been made at frequencies from 1.4 to 18 GHz. We draw the following conclusions from our observations:

- G64.5+0.9 is confirmed as a shell SNR and its emission follows a power-law spectrum with $\alpha = 0.47 \pm 0.03$;
- by considering its size, shape and spectral behaviour, and a probabilistic analysis using NVSS radio source counts, we argue that the emission apparently at the centre of the ring is most unlikely to be any kind of extragalactic radio source;
- it is difficult to avoid the conclusion that the apparently central emission is associated with the shell, although its spectrum is very unlike that of a pulsar wind nebula, and it therefore merits further investigation, particularly follow-up HI absorption line observations.

7 ACKNOWLEDGMENTS

We thank the staff of the Mullard Radio Astronomy Observatory for their invaluable assistance in the commissioning and operation of AMI, which is supported by Cambridge University and the STFC. MLD, TMOF, CRG, NHW and TWS acknowledge the support of PPARC/STFC studentships.

REFERENCES

- AMI Consortium: Zwart et al., 2008, MNRAS, 391, 1545
 Baars J. W. M., Genzel R., Pauliny-Toth I. I. K., Witzel A., 1977, A&A, 61, 99
 Boland J. W., Hollinger J. P., Mayer C. H., McCullough T. P. 1966, ApJ, 144, 437
 Browne I. W. A., Wilkinson P. N., Patnaik A. R., Wrobel J. M., 1998, MNRAS, 293, 257
 Brunetti et al., 2008, Natur, 455, 944B
 Condon J. J., Cotton W. D., Greisen E. W., Yin Q. F., Perley R. A., Taylor G. B., Broderick J. J., 1998, AJ, 115, 1693
 Dickel J. R., Milne D. K. and Strom R. G., 2000, ApJ, 115, 1693

⁶ http://sundog.stsci.edu/first/catalog_paper/node6.html

- Fanaroff B. L. and Riley, J. M., 1974, MNRAS, 167P, 31F
Green D. A., 2001, MNRAS, 326, 283G
Green D. A., 2004, BASI, 32, 335
Green D. A., 2007, BASI, 35, 77
Kotthes R., Landecker T. L., Reich W. and Safi-Harb S., 2008, ApJ, 687, 518
Manchester R. N., Hobbs G. B., Teoh A., Hobbs M., 2005, AJ, 129, 1993-2006
IRAS Catalogues and Atlases: The Point Source Catalog, 1987, eds. C. A. Bechman, G. Neugebauer, H. J. Habing, P. E. Clegg, T. J. Chester, NASA RP-1190
Patnaik A. R., Browne I. W. A., Wilkinson P. N., Wrobel J. M., 1992, MNRAS, 254, 655
Reich W., Fürst E., Haslam C. G. T., Steffen P., Reif K., 1984, A&AS, 58, 197
Taylor A. R., Goss W. M., Coleman P. H., van Leeuwen J., Wallace B. J., 1996, ApJS, 107, 239
Taylor A. R. et al., 2003, AJ, 125, 3145
Tian W. W. and Leahy D. A., 2006, AJ, 455, 1053
Wilkinson P. N., Browne I. W. A., Patnaik A. R., Wrobel J. M., Sorathia B., 1998, MNRAS, 300, 790

This paper has been typeset from a $\text{\TeX}/\text{\LaTeX}$ file prepared by the author.